Materials & Design 210 (2021) 110060

Contents lists available at ScienceDirect

Materials & Design

journal homepage: www.elsevier.com/locate/matdes

Promoting polysulfides redox conversion by sulfur-deficient ZnS_{1-x} hollow polyhedrons for lithium-sulfur batteries

Wanjie Gao [a], Qianwen Jin [a], Yanyu Liu [a], Yongguang Zhang [a,*], Xin Wang [b,*], Zhumabay Bakenov [c]

[a] School of Materials Science and Engineering, State Key Laboratory of Reliability and Intelligence of Electrical Equipment, Hebei University of Technology, Tianjin 300130, China
[b] South China Academy of Advanced Optoelectronics & International Academy of Optoelectronics at Zhaoqing, South China Normal University, Guangzhou 510006, China
[c] Department of Chemical and Materials Engineering, National Laboratory Astana, Nazarbayev University, Institute of Batteries LLP, Nur-Sultan 010000, Kazakhstan

HIGHLIGHTS

- The sulfur-deficient ZnS_{1-x} hollow polyhedrons are synthesized by the sulfurization and high-temperature annealing method.
- The hollow structure could accommodate volumetric change during cycling and physically suppress the polysulfides shuttling.
- The sulfur vacancies in ZnS_{1-x} could enhance polysulfides adsorption and accelerate polysulfides redox conversion.
- The S/ZnS_{1-x} cathode exhibits the favorable rate capability and excellent cycling performance.

GRAPHICAL ABSTRACT

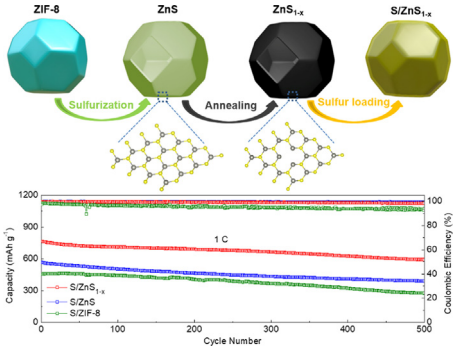

ARTICLE INFO

Article history:
Received 2 June 2021
Revised 18 August 2021
Accepted 20 August 2021
Available online 21 August 2021

Keywords:
Sulfur-deficient
Hollow structure
Sulfur host
Polysulfides redox conversion
Lithium-sulfur battery

ABSTRACT

Lithium-sulfur (Li-S) batteries are deemed as the attractive systems for high-energy storage. However, the polysulfides shuttling with slow redox kinetics has seriously hindered their practical applications. Herein, sulfur-deficient zinc sulfide (ZnS_{1-x}) hollow polyhedrons are synthesized as the multifunctional sulfur host material via the sulfurization and high-temperature annealing method. The unique hollow structure could supply adequate void spaces for sulfur loading and alleviate volumetric expansion of sulfur upon the cycling process. Besides, ZnS_{1-x} hollow polyhedrons with abundant sulfur vacancies can provide effective adsorption sites to chemically immobilize polysulfides and enhance polysulfides redox conversion as confirmed by theoretical calculation results and electrocatalytical experiments. Thus, the S/ZnS_{1-x} cathode delivers the remarkable initial capacity (1206 mAh g^{-1} at 0.2 C) and excellent cycling stability (592 mAh g^{-1} after 500 cycles at 1 C). The study points out the idea of functional cathode material for Li-S batteries based on a simple yet efficient vacancy engineering method.

1. Introduction

The growing demands for renewable energy have stimulated numerous researches on advanced energy storage systems [1,2]. Lithium-sulfur (Li-S) batteries have emerged as the competitive candidate because of the favorable energy density (2600 Wh kg^{-1}), non-toxicity and low cost of sulfur [3–6]. However, their commercial applications have been seriously hindered by several obstacles: (1) the insulating property of S and lithium sulfide (Li_2S_2/Li_2S) may lead to the low utilization of sulfur [7,8]; (2) the huge volume change (~80%) of sulfur upon charge/discharge process may destroy the integrity of electrode [9,10]; and (3) the seri-

* Corresponding authors.
E-mail addresses: yongguangzhang@hebut.edu.cn (Y. Zhang), wangxin@scnu.edu.cn (X. Wang).

https://doi.org/10.1016/j.matdes.2021.110060
0264-1275/

ous shuttling effect of soluble polysulfides (Li_2S_n, $4 \leq n \leq 8$) may result in high consumption of electrical energy and longer charging time than discharging time. The time-dependent heat accumulation also will lead to inferior electrochemical performance and poor safety [11,12].

To handle the aforementioned obstacles, recent research efforts have been devoted to developing functional cathode host materials with optimized configurations. Currently, carbon materials [13], metal oxides/sulfides/nitrides [14–18], metal organic frameworks (MOFs) [19,20], and covalent organic frameworks (COFs) [21,22] have been adopted to act as cathode host materials of Li-S batteries. Particularly, various carbon materials with high conductivity and distinctive structures have been widely applied to design efficient sulfur hosts. Nevertheless, nonpolar carbon materials may not inhibit lithium polysulfides (LiPSs) dissolution and shuttling since they only show weak physical interaction with polar polysulfides [23–26]. To overcome this, some polar materials including metal oxides/sulfides/nitrides and MOFs could anchor polysulfides on the polar interface by strong chemical adsorption. Among them, because of the weak ionic property of metal-sulfur bond and reduced electron localization, metal sulfides possess excellent electronic conductivity [27,28]. Besides, metal sulfides also can provide chemical adsorption sites to improve sulfur utilization, effectively anchor LiPSs and catalyze LiPSs conversion, resulting in excellent cycling performance for Li-S batteries [29,30]. For example, Xu et al. synthesized a conductive hollow Co_3S_4 polyhedra, which act as the functional sulfur cathode material to accelerate sulfur redox kinetics and inhibit polysulfides shuttling in Li-S batteries [31].

Nowadays, intensive research has considered the alternative of enhancing the polysulfides conversion kinetics in the sulfur cathode [32,33]. In this aspect, structural design and defect engineering are regarded as the favorable strategies to accelerate the conversion of polysulfides [34–36]. Furthermore, defects such as sulfur vacancies are also the most reactive sites on the surfaces of metal sulfides. Sulfur vacancies are also well-known to enhance the intrinsic conductivity of metal sulfides and promote the sulfur redox kinetics [37–39]. For instance, Lee et al. designed two-dimensional layer-structured MoS_2 nanoflakes with sulfur vacancies as sulfur cathode material in Li-S batteries, showing strong chemical interaction to polar polysulfides and excellent catalytic effect for polysulfides conversion [40].

Herein, we report ZnS_{1-x} hollow polyhedrons with abundant sulfur vacancies as sulfur host material of Li-S batteries. The unique hollow structure can not only supply a sufficient void for sulfur accommodation and prevent volume variation of sulfur during lithiation process, but also inhibit the migration and diffusion of LiPSs physically. It is also verified that the surface sulfur vacancies participate in the polysulfides adsorption and promote electrochemical redox reactions of LiPSs. Consequently, the S/ZnS_{1-x} cathode shows the reversible initial discharge capacity (1206 mAh g^{-1} at 0.2 C) and outstanding rate capability (549mAh g^{-1} at 4 C). These results not only supply direct evidence for the contribution of sulfur vacancy on the catalytic activity of ZnS in the polysulfides redox conversion, but also supply a strategy for how to deploy catalysts in Li-S batteries to obtain the best catalytic results.

2. Experimental section

2.1. Preparation of ZIF-8

$Zn(NO_3)_2{\cdot}6H_2O$ (3.67 g) was dissolved into 250 mL of anhydrous methanol to prepare solution A. 2-methylimidazole (4.05 g) and 1-methylimidazole (2.5 g) were dissolved into 250 mL of anhydrous methanol to prepare solution B. Then the two solutions were mixed, stirred for 30 min and left to stand for 24 h. After that, the sample was centrifuged three times each with anhydrous ethanol and dried in an 65 °C oven.

2.2. Preparation of ZnS and ZnS_{1-x}

ZIF-8 (0.2 g) and thioacetamide (10 g) were dissloved in 150 and 100 mL of anhydrous ethanol, respectively. Then the two solutions were mixed, stirred for 30 min and heated in oil bath at 120 °C for 60 min. After that, the solid ZnS was centrifuged three times each with anhydrous ethanol and dried in an 65 °C oven. Finally, the synthesis of ZnS_{1-x} by calcining ZnS at 500 °C for 5 h in a 10% H_2/Ar atmosphere.

2.3. Preparation of S/ZnS_{1-x} composite

The ZnS_{1-x} and sulfur (weight ratio = 1:4) were mixed, heated to 155 °C and kept for 12 h in flowing argon. After cooling down, the S/ZnS_{1-x} composite was collected. For experimental comparisons, S/ZnS and S/ZIF-8 were obtained by using the identical method.

2.4. Structural characterization

The materials crystallography was recorded by X-ray diffraction (XRD, Rigaku DLMAX-2550 V) operated using Cu Kα radiation. The morphology and structure of sample was recorded by scanning electron microscopy (SEM, FEI, XL30 Sirion). The material microstructure was analyzed by transmission electron microscopy (TEM, TF30ST-300 kV). The sulfur content of S/ZnS_{1-x} composite was calculated on a thermogravimetric analysis (TGA, NETZSCH STA449C) in flowing N_2. The Brunauer-Emmett-Teller (BET) surface area and pore size distribution were measured by the Micromeritics ASAP 2020 analyzer. The X-ray photoelectron spectroscopy (XPS, K-Alpha 1063) was applied to analyze the surface chemistry of the samples. Electron paramagnetic resonance (EPR) measurement was analyzed by using an Endor spectrometer (Bruker A300) at 77 K. The UV–Visible results were collected by a Shimadzu UV-3600 spectroscopy.

2.5. Electrochemical characterization

The S/ZnS_{1-x}, super P, and polyvinylidene fluoride (PVDF) (weight ratio = 8:1:1) were mixed, ground and dispersed in N-methyl-pyrrolidone (NMP), then obtained slurry was coated on the Al foil and dried in a 60 °C oven. After that, the electrodes were cut into 12 mm-diameter discs. The actual sulfur loading was about 2 mg cm^{-2}. For experimental comparisons, S/ZnS and S/ZIF-8 cathodes were prepared by the identical procedure. The CR2032 coin cells were assembled by using Li foil as anode, Celgard 2400 as separator in an Ar-filled glovebox. The electrolyte was prepared by dissolving 1.0 mol L^{-1} lithium bis-trifluoromethane sulfonylimide (LiTFSI) and 0.1 mol L^{-1} lithium nitrate ($LiNO_3$) in 1,3-dioxolane/1,2-dimethoxymethane (DOL/DME) (1:1 v/v). About 60 μL electrolyte was used to assemble each coin cell. The cyclic voltammetry (CV) curves and electrochemical impedance spectroscopy (EIS) plots were analyzed by using CHI660C electrochemical workstation. The battery cycling performances and rate capability can be studied by using a Neware Battery Measurement System (Neware, China) with a cutoff voltage 1.7–2.8 V.

2.6. Adsorption experiments

The Li_2S_6 solution was gained by dissolving Li_2S and S (molar ratio = 1:5) into DOL/DME (1:1 v/v) at 60 ℃ under vigorous stirring for 24 h. Then, 5 mg ZnS_{1-x}, ZnS and ZIF-8 was added into the 3 mL

Li_2S_6 solution (3 mM), respectively. The whole process was conducted on an Ar-filled glovebox.

2.7. Symmetric cell tests

The ZnS_{1-x} (or ZnS, or ZIF-8) and PVDF (weight ratio = 9:1) was mixed and dispersed in NMP. After that, the gained slurry was casted on carbon cloth and dried at 60 °C. Finally, the electrodes were cut into 12 mm-diameter discs. The electrolyte was made by adding 0.1 M Li_2S_6 in DOL/DME (1:1 by v/v). The symmetric cells were assembled using prepared electrodes as the working and the counter electrodes and Celgard 2400 as separator. The CV and EIS tests were studied by the VSP-300 electrochemical workstation.

2.8. Li_2S nucleation tests

The Li_2S_8 solution was prepared by dissolving Li_2S and S (molar ratio = 1:7) into a tetraglyme solution at 60 °C with vigorous stirring overnight. The ZnS_{1-x} (or ZnS, or ZIF-8) was added to ethanol and then dispersed on carbon cloth. The Li-catalyst electrochemical cells were assembled using the above carbon cloth as cathode, Li metal as anode and Celgard 2400 as separator. The cells were galvanostatically discharged to 2.06 V under 0.112 mA and then the voltage would be held at 2.05 V until the current dropped to 0.01 mA.

2.9. Theoretical calculations

Density functional theory (DFT) calculations were conducted using the Vienna Ab initio Simulation Package (VASP), with the project-augmented wave (PAW) potential. The exchange-correlation functional used is the Perdew-Burke-Ernzerhof (PBE) of generalized gradient approximation (GGA) with a cutoff energy of 400 eV. The ZnS was modelled using ZnS (1 1 1) surface and the sulfur vacancies by removing several neighbouring S atoms. A k-point mesh of $3 \times 3 \times 1$ was used for the Brillouin-zone integrations. The vacuum height is set to 15 Å. A maximum force tolerance of 0.01 eV $Å^{-1}$, and a maximum displacement tolerance of 5.0×10^{-4} Å are used for all calculations.

3. Results and discussion

The preparation procedure of S/ZnS_{1-x} composite is exhibited in Fig. 1. The chemically unstable metal-organic framework can be transformed into the various structure by distinctive reaction with specific substance. In this regard, the zeolitic imidazolate framework 8 (ZIF-8) with a truncated octahedral shape is used to prepare ZnS hollow polyhedrons by a simple sulfurization process. The sulfurization reaction results in the occurrence of one outer shell. Then the internal kernel of ZIF-8 particles is shrunk. Simultaneously, the central quality is moved outward driven by the reaction between Zn^{2+} cations that are slowly dissolved from ZIF-8 template and S^{2-} anions that are liberated during hydrolysis of thioacetamide [41,42]. Afterward, the ZnS_{1-x} hollow polyhedrons are synthesized by calcining the ZnS under a 10% H_2/Ar atmosphere. Finally, sulfur is incorporated into the ZnS_{1-x} hollow polyhedrons to fabricate S/ZnS_{1-x} composite via a conventional melt-diffusion method.

The structure and morphology of ZIF-8 template particles are illustrated in Fig. 2a. It displays the well-defined truncated octahedron shape with a smooth surface, in which the size distribution remains uniform and the particle diameter is about 1-2 μm on average. The uniform ZnS polyhedrons are exhibited in Fig. 2b. The ZnS polyhedrons maintain the truncated octahedron shape resembling the precursor MOF although with a larger inner cavity. This hollow structure can also be observed (inset in Fig. 2b) as one can find that its edges are darker and the interior is lighter. Compared with ZnS, the SEM images of ZnS_{1-x} indicate good morphology maintenance (Fig. 2c,d). The evenly distributed ZnS_{1-x} with hollow structure could provide a huge space to restrict the volume change during cycling and isolate LiPSs from electrolyte. As shown in Fig. 2e, the unique hollow structure for ZnS_{1-x} can be further verified by TEM image. The ZnS_{1-x} hollow polyhedrons still keep the truncated octahedron shape. The crystalline feature of the ZnS_{1-x} is shown by HRTEM images (Fig. 2f). The crystallized feature of ZnS can be indicated by the Fast Fourier transform (FFT) pattern and inverse FFT analysis. Subsequently, the inverse FFT patterns can establish the (1 1 1) plane of ZnS (Fig. 2g,h). The neatly arranged lattice stripes (Fig. 2g, red frame) exhibit the 0.313 nm interplanar spacing. Furthermore, relatively disordered lattices (Fig. 2h, yellow frame) in ZnS_{1-x} can be detected. The interplanar spacing can be increased to 0.315 nm, exhibiting the disorderly lattice because of the introduction by sulfur vacancies. This disorder structure enables to supply active sites to carry charge and influence its fast reorganization for enhancing the charge transfer capability. The elemental mappings of ZnS_{1-x} hollow polyhedrons clearly (Fig. 2i-l) indicate that Zn and S are evenly distributed in the complete hollow polyhedrons.

As shown in Fig. 3a, the XRD analysis of ZnS indicates typical characteristic peaks at 28.5°, 47.6° and 56.3°, which are consistent with (1 1 1), (2 2 0) and (3 1 1) crystalline plane of ZnS (JCPDS NO. 77-2100). Notably, a negative shift can be noticed for ZnS_{1-x} compared with ZnS (inset in Fig. 3a), exhibiting the increase of lattice parameters owing to the introduction of defect engineering. Besides, XRD pattern of S/ZnS_{1-x} indicates characteristic peaks of sulfur (JCPDS No. 08-0247), exhibiting that sulfur is successfully loaded on ZnS_{1-x} (Fig. 3b). The EPR spectra also can be carried out to further verify the formation of sulfur vacancies. According to Fig. 3c, ZnS_{1-x} displays a strong EPR signal with a g-value of 2.00, while weak signal is shown in ZnS, which further verifies the existence of sulfur vacancies in ZnS_{1-x}. The XPS spectra is used to analyze the surface chemical composition of the samples. The Zn 2p spectra of ZnS indicates two peaks of Zn $2p_{3/2}$ and Zn $2p_{1/2}$ at 1022.8 and 1045.8 eV, respectively, corresponding to the valence feature of Zn^{2+} (Fig. 3d). Compared with ZnS, these peaks in ZnS_{1-x} move towards the lower values (1022.2 eV and 1045.3 eV)

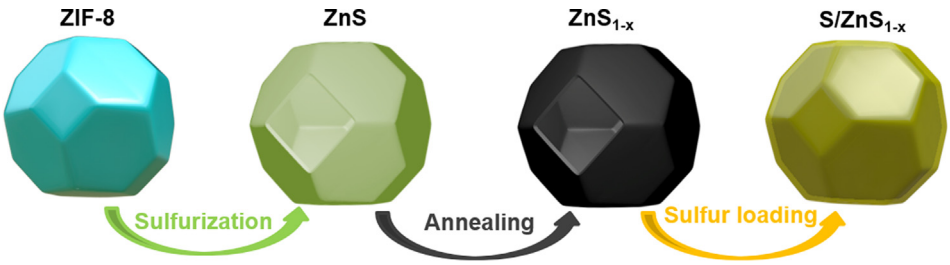

Fig. 1. Schematic of the synthesis of the S/ZnS_{1-x}.

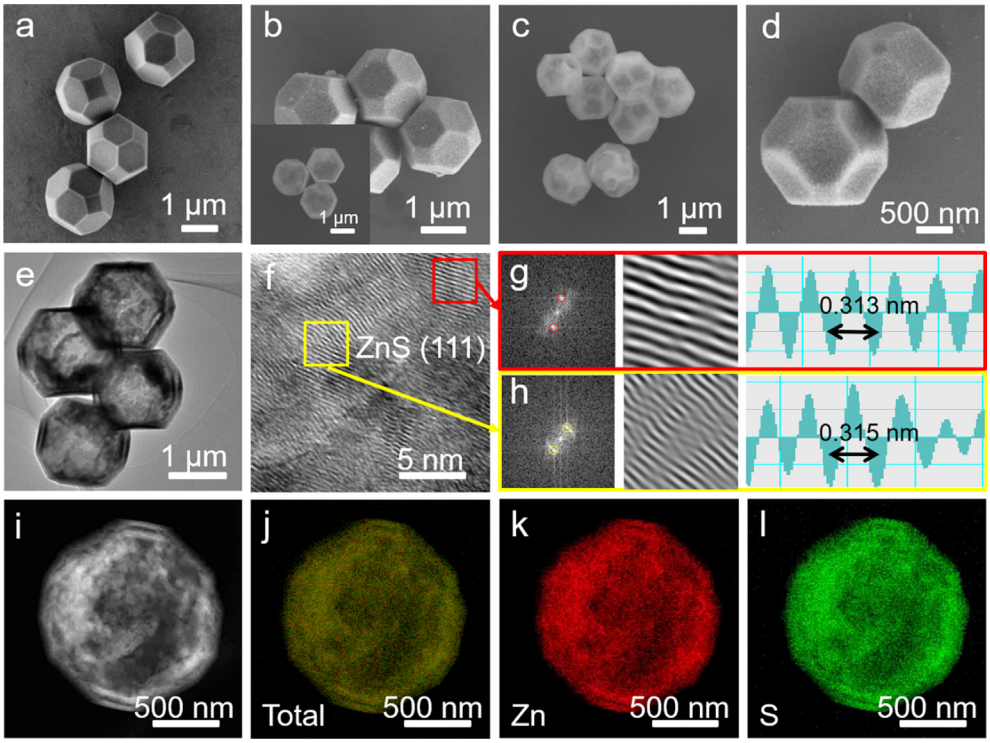

Fig. 2. (a) SEM image of ZIF-8; (b) SEM image of ZnS (inset is a SEM image under high-voltage of 20 kV); (c, d) SEM images of ZnS_{1-x} under different voltages; (e) TEM image, (f) HRTEM image, (g,h) FFT images and the lattice spacing profiles along the selected areas, (i-l) EDS elemental mapping of ZnS_{1-x}.

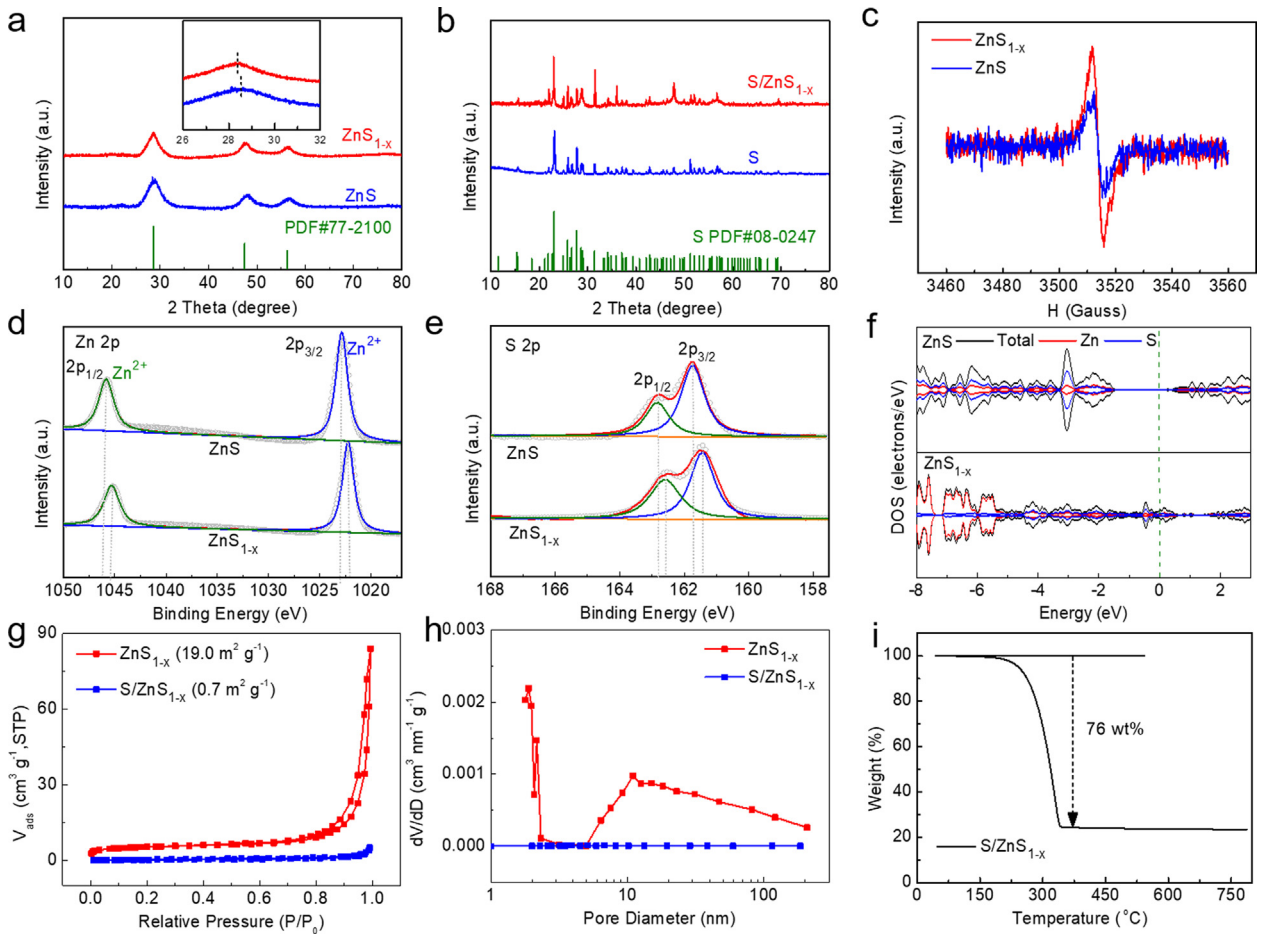

Fig. 3. (a) XRD patterns of ZnS_{1-x} and ZnS; (b) XRD patterns of S/ZnS_{1-x} and S; (c) EPR tests, (d) Zn 2p XPS spectra, (e) S 2p XPS spectra and (f) DOS patterns of ZnS_{1-x} and ZnS; (g) Isotherm curves and (h) pore size distribution of ZnS_{1-x} and S/ZnS_{1-x}; (i) TGA curve of S/ZnS_{1-x}.

because of the formation of sulfur vacancies [43]. In addition, the S 2p XPS spectra (Fig. 3e) indicates that the characteristic peaks of ZnS_{1-x} shift to lower value compared with ZnS. The sulfur vacancies engineering enables to accelerate the electron conduction and change the electronic structure, which can be verify by the density of states (DOS). Compared with ZnS, the DOS of ZnS_{1-x} shows a narrower bandgap, demonstrating the enhanced electron conduction by the abundant sulfur vacancies (Fig. 3f). In addition, the BET surface area (19.0 $m^2\ g^{-1}$) and pore size distribution of the ZnS_{1-x} are indicated by the N_2 adsorption-desorption isotherm curves (Fig. 3g,h). After sulfur loading, the S/ZnS_{1-x} composite exhibit a surface area of 0.7 $m^2\ g^{-1}$, indicating that sulfur was successfully loaded on ZnS_{1-x}. Similarly, the decrease in BET surface areas of S/ZnS and S/ZIF-8 also indicate the successful loading of sulfur onto ZnS and ZIF-8, respectively (Fig. S1). The sulfur content in S/ZnS_{1-x} composite is calculated to be 76 wt% using TGA analysis under N_2 atmosphere (Fig. 3i).

Fig. 4 shows the electrochemical characterizations of the three different cathodes. CV curves of the three cathodes (Fig. 4a) demonstrate that S/ZnS_{1-x} cathode indicates the highest current response and the smallest polarization, exhibiting that S/ZnS_{1-x} can improve sulfur utilization and effectively boost polysulfides conversion kinetics. Fig. 4b exhibits the charge/discharge curves of S/ZnS_{1-x} cathode under different cycles at 0.2 C. Obviously, all voltage profiles show two typical discharge platforms and a charging slope, which corresponds to CV curves. After 100 cycles, it can be noted that charge/discharge profile is maintained, exhibiting the restricted LiPSs shuttle effect and stable cycle capability. As presented in Fig. 4c, the S/ZnS_{1-x} cathode delivers a remarkable initial capacity of 1206 mAh g^{-1} at 0.2 C with a about 99% coulombic efficiency. After 100 cycles, the capacity retention (81%) of S/ZnS_{1-x} cathode is higher than those of S/ZnS (66%) and S/ZIF-8 (55%) cathodes. The rate capability of the three cathodes are displayed in Fig. 4d. Clearly, the S/ZnS_{1-x} cathode manifests the discharge capacities of 1224, 926, 805, 687, 606 and 549 mAh g^{-1} at 0.2, 0.5, 1, 2, 3 and 4 C, respectively. It can maintain the 945 mAh g^{-1} discharge capacity when the current rate returns to 0.2 C, suggesting the excellent cycle reversibility in S/ZnS_{1-x} cathode. Moreover, Fig. 4e indicates the discharge/charge curves of S/ZnS_{1-x} cathode under different rates from 0.2 to 4 C. Obviously, the S/ZnS_{1-x} cathode exhibits two discharge plateaus and one charge plateau, which corresponds to the CV curves. Fig. 4f shows the EIS spectrum obtained with the Li-S batteries fabricated with S/ZnS_{1-x}, S/ZnS and S/ZIF-8 cathodes, respectively. The corresponding equivalent circuit is displayed as the inset of Fig. 4f. As listed in Table S1, the charge transfer resistance (Rct) of S/ZnS_{1-x} cathode (42.9 Ω) is smaller than those of the S/ZnS (62.2 Ω) and S/ZIF-8 (123.2 Ω) cathodes, exhibiting the enhanced electron/ion transfer owing to defect-rich ZnS_{1-x} architecture. Fig. 4g presents the long cycle performances of the different cathodes. The S/ZnS_{1-x} cathode shows a high specific capacity of 766 mAh g^{-1} at 1 C, after 500 cycles, it also maintains a discharge capacity of 592 mAh g^{-1} with a low capacity decay rate of 0.045% per cycle. By contrast, S/ZnS and S/ZIF-8 cathodes show fast capacity fading at 1 C. As a result,

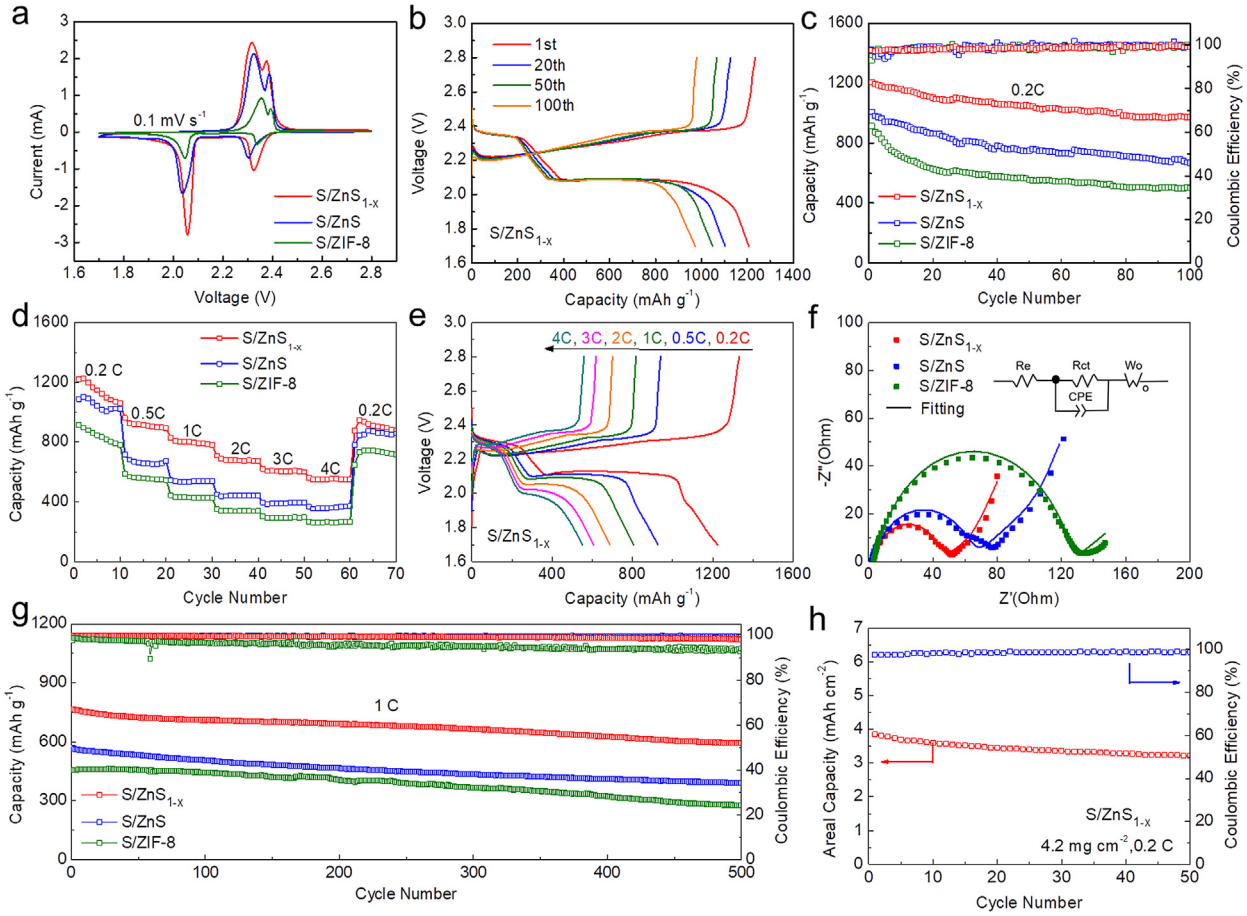

Fig. 4. (a) CV curves at 0.1 mV s^{-1} of S/ZnS_{1-x}, S/ZnS and S/ZIF-8 cathodes; (b) Discharge/charge curves of S/ZnS_{1-x} cathode at 0.2 C; (c) Cycling performance at 0.2 C of S/ZnS_{1-x}, S/ZnS and S/ZIF-8 cathodes; (d) Rate capability of S/ZnS_{1-x}, S/ZnS and S/ZIF-8 cathodes; (e) Discharge/charge curves of S/ZnS_{1-x} cathode under different rates; (f) Nyquist diagrams (inset: equivalent circuit models) and (g) Long-cycling tests at 1 C of S/ZnS_{1-x}, S/ZnS and S/ZIF-8 cathodes; (h) Cycling performance at high sulfur loadings for S/ZnS_{1-x} cathode at 0.2 C.

the excellent cycle capability of the S/ZnS_{1-x} cathode can be ascribed to rapid electron/ion transfer, excellent LiPSs affinity and good electrical conductivity of the defect-rich ZnS_{1-x}, which immobilizes LiPSs and catalyzes LiPSs conversion kinetics, resulting in the favorable inhibition on shuttle effect. Besides, the practical application of Li-S batteries requires an excellent electrochemical performance under high sulfur loading. As shown in Fig. 4h, the S/ZnS_{1-x} cathode shows the initial areal discharge capacity of 3.85 mAh cm^{-2} under the raised sulfur loading of 4.2 mg cm^{-2}, which still maintains of 3.21 mAh cm^{-2} after 50 cycles at 0.2 C, exhibiting the excellent kinetic improvement accomplished by the architectural design and defect engineering. Beyond that, the as-developed S/ZnS_{1-x} cathode also exhibits a relatively excellent performance among the recently reported ZnS-based cathodes (Table S2), further verifying its favorable structural benefits. The above results strongly confirm the great superiorities of the unique hollow ZnS_{1-x} design in promoting and stabilizing sulfur reactions for advanced Li-S batteries.

The visualized adsorption experiments are carried out to explore the adsorption effect of the different samples on polysulfides. The color of the Li_2S_6 solution becomes visually colorless after adding ZnS_{1-x}, while ZnS and ZIF-8 exhibits the weak adsorption capability to decolor Li_2S_6 solution (inset in Fig. 5a). The corresponding UV–vis absorption spectra (Fig. 5a) indicates the lowest LiPSs related absorption peaks, confirming the strongest adsorption capability of ZnS_{1-x}. In addition, XPS spectrum can be used to further study the interaction mechanism between Li_2S_6 and ZnS_{1-x}. The Zn 2p XPS spectrum (Fig. 5b) indicates that the binding energy of peaks of Li_2S_6@ZnS_{1-x} shifts to higher values compared with ZnS_{1-x}. This result reveals that sulfur species from LiPSs refill sulfur vacancies to achieve chemical adsorption of Li_2S_6 on ZnS_{1-x} [41]. Apart from the adsorption experiments, enhanced redox kinetics can be evaluated by Li^+ diffusion property. Fig. 5c-e show the Li^+ diffusion energy profiles and the corresponding geometrical configurations on ZnS and ZnS_{1-x} surfaces. Compared with that on ZnS (0.53 eV), the lower diffusion barrier energy of 0.29 eV can be noticed by the sulfur-deficient ZnS_{1-x} surface, displaying the enhanced ion transfer by the sulfur vacancies. To further study the underlying interaction between polysulfides and ZnS_{1-x}, DFT calculations are carried out to analyze Li_2S_6 adsorption on ZnS (1 1 1) and ZnS_{1-x} (1 1 1) surfaces. The optimized configuration of Li_2S_6 adsorption capability on ZnS and ZnS_{1-x} was shown in Fig. 5f, g. The Li_2S_6 indicates a stronger binding energy of −3.91 eV on ZnS_{1-x} surface compared with that on ZnS surface (-2.38 eV), demonstrating the better LiPSs affinity of ZnS_{1-x}. These excellent adsorption behaviors are beneficial for immobilizing sulfur and inhibiting the LiPSs shuttle effect in Li-S configuration.

The Li^+ diffusion coefficient (D_{Li+}) can confirm that the ZnS_{1-x} with abundant sulfur vacancies can accelerate LiPSs conversion kinetics. The CV profiles of three sulfur cathodes at different scan rates can be used to study D_{Li+}. Fig. 6a-c show the CV profiles of the different cathodes at first three cycles, respectively. The three

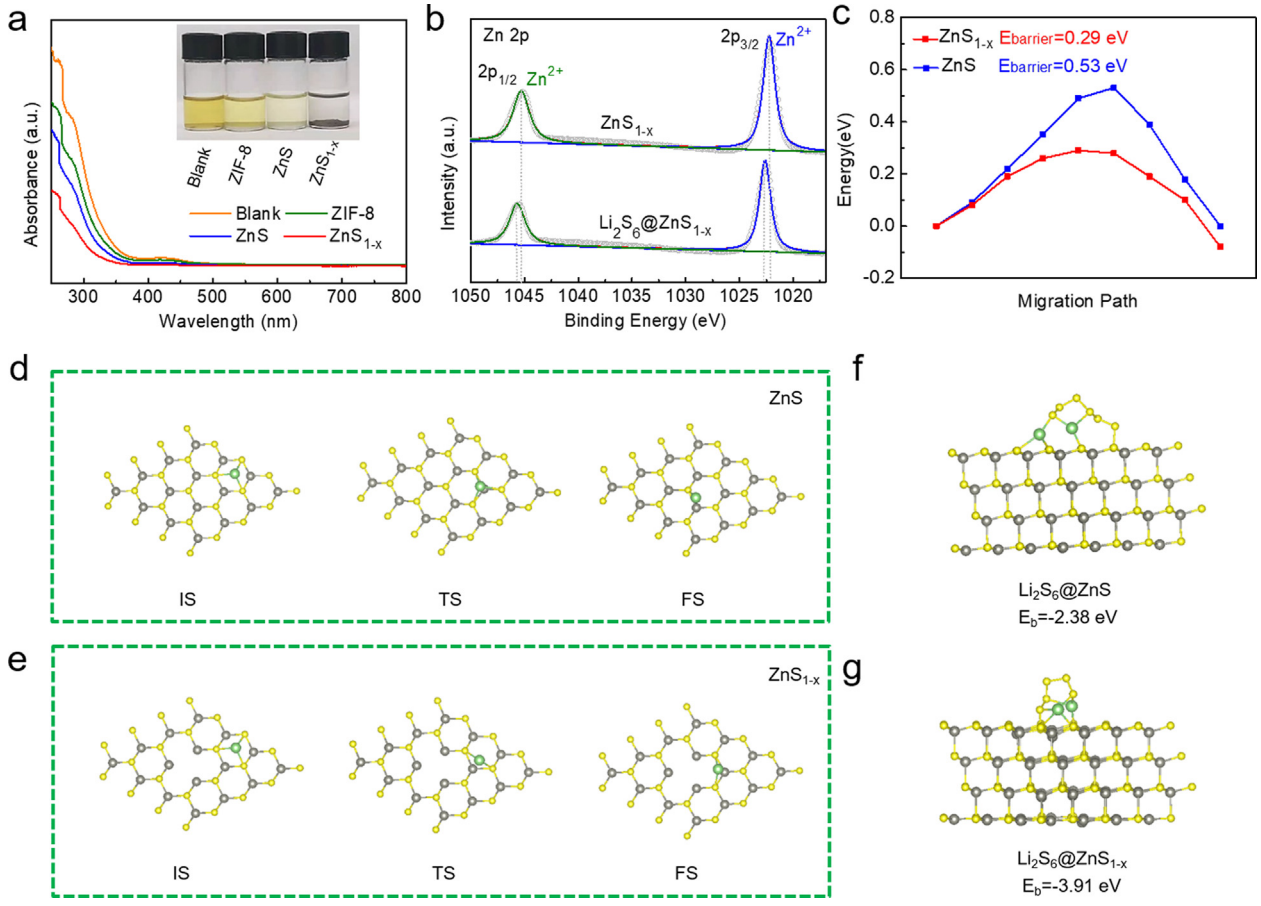

Fig. 5. (a) Optical image of Li_2S_6 adsorption by ZnS_{1-x}, ZnS and ZIF-8 and the corresponding UV–vis spectra; (b) Zn 2p spectra in ZnS_{1-x} before and after Li_2S_6 adsorption; (c) Li^+ diffusion energy profiles and (d,e) the geometrical configurations of Li^+ diffusion on ZnS and ZnS_{1-x} surfaces; (f,g) Optimized configuration of Li_2S_6 adsorption on ZnS and ZnS_{1-x}. The green, gray and yellow balls represent Li, Zn and S atoms, respectively. (For interpretation of the references to color in this figure legend, the reader is referred to the web version of this article.)

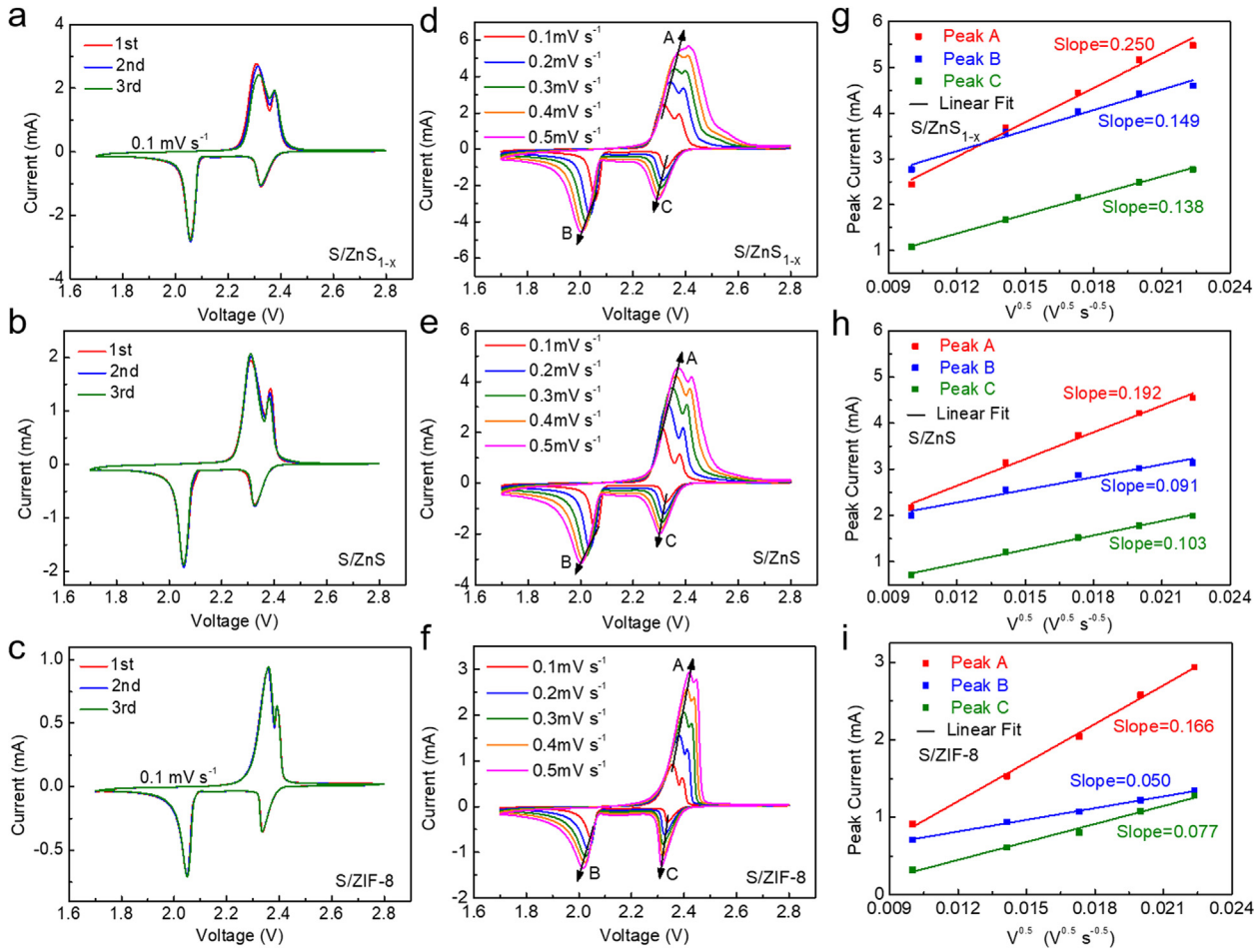

Fig. 6. (a-c) CV curves under first three cycles, (d-f) CV rate curves and (g-i) corresponding liner plots of peak currents vs. square root of the scan rate ($V^{0.5}$) of S/ZnS_{1-x}, S/ZnS and S/ZIF-8 cathodes.

cathodes display two cathodic peaks at about 2.3 V and 2.05 V, corresponding to the transformation of S_8 to long-chain Li_2S_n ($4 \leq n \leq 8$) and the further reduction of long-chain Li_2S_n to short-chain Li_2S_2/Li_2S, respectively. The two anodic peaks at about 2.3 and 2.4 V represent the reverse transformation of Li_2S/Li_2S_2 to short-chain LiPSs and finally to S_8. The CV profiles of the three different cathodes in the initial three cycles are well-overlapped, exhibiting its high electrochemical reversibility. Based on the Li^+ diffusion coefficient, the CV profiles under various scan rates can be used to explore catalytic effect of ZnS_{1-x} (Fig. 6d-f). According to the Randles-Sevick equation, for all three peaks, the slopes of the S/ZnS_{1-x} cathode are higher than those of S/ZnS and S/ZIF-8 cathodes, demonstrating the facilitated Li^+ diffusion characteristic in the sulfur-deficient ZnS_{1-x} (Fig. 6g-i). The enhanced Li^+ transfer can accelerate polysulfides conversion kinetics during the Li^+ insertion/extraction processes.

The symmetric cells tests can be used to verify the catalytic activity on the LiPSs redox conversion. The CV curves of symmetrical cells with a cutoff voltage −1.5 V-1.5 V are presented in Fig. 7a. Obviously, the ZnS_{1-x} electrode displays the highest current response and narrowest peak separation compared with those of ZnS and ZIF-8 electrodes, confirming the facilitated LiPSs conversion kinetics. The well-overlapped CV profiles under different cycles also indicates excellent cycle reversibility of the ZnS_{1-x} electrode (Fig. 7b). The nyquist plot of symmetric cells can also verify improved redox kinetics in ZnS_{1-x} electrode. Apparently, the charge transfer resistance of the ZnS_{1-x} electrode is smaller than those of ZnS and ZIF-8 electrodes (Fig. 7c), confirming its rapid charge transfer process. Furthermore, Fig. 7d-f shows CV curves of symmetric cells using three electrodes under various scan rates. Obviously, the ZnS_{1-x} electrode indicates the smaller potential gap between the redox peaks than those of ZnS and ZIF-8 electrodes, further exhibiting the enhanced polysulfides conversion kinetics and excellent catalytic performance of as-developed ZnS_{1-x}. Besides, the Li_2S precipitation behaviors are investigated to verify catalytic performance in different surface (Fig. 7g-i). The ZnS_{1-x} electrode shows the higher Li_2S precipitation capacity (125 mAh g^{-1}) than those of ZnS (94 mAh g^{-1}) and ZIF-8 (66 mAh g^{-1}), demonstrating significantly enhanced Li_2S nucleation and precipitation behaviors on the ZnS_{1-x} surface.

Linear sweep voltammetry (LSV) tests are conducted on three-electrode device to investigate the Li_2S oxidization behavior (Fig. 8a). Compared with glassy carbon, ZnS and ZIF-8 electrodes, the ZnS_{1-x} electrode shows the largest current response, demonstrating the excellent catalytic performance by defect-rich ZnS_{1-x}. The Li_2S decomposition also can be studied by DFT calculation. This calculation can be used to explore the mechanism of the kinetic improvement. According to Fig. 8b, compared with ZnS (1.77 eV), it is noteworthy that ZnS_{1-x} achieve a smaller energy barrier of 0.88 eV for the Li_2S decomposition, which verifies that the enhanced Li_2S redox reactions on the ZnS_{1-x} surface. In addition, Fig. 8c, d show the corresponding geometrical configurations on

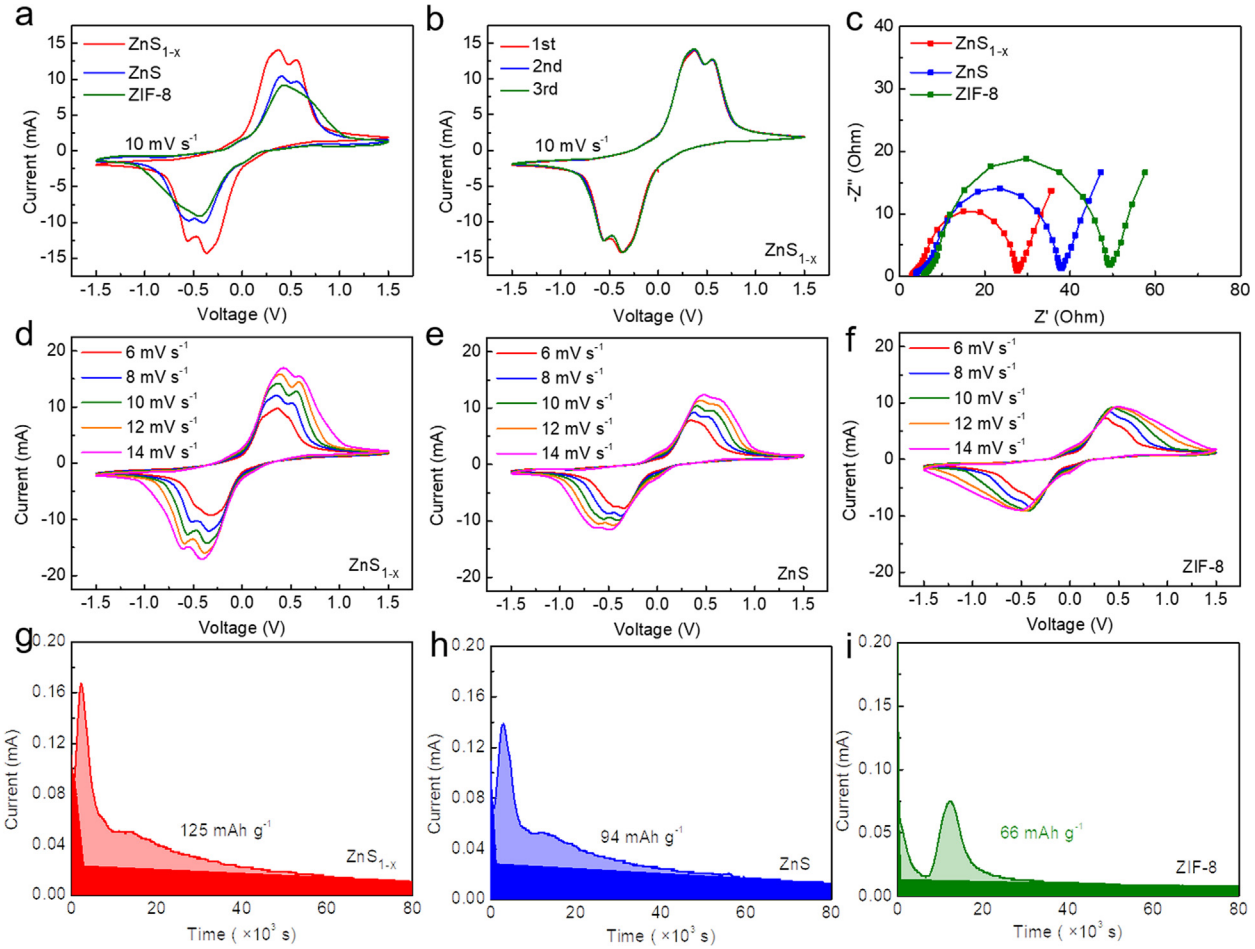

Fig. 7. (a) CV curves of ZnS_{1-x}, ZnS and ZIF-8 symmetric cells; (b) CV curves of ZnS_{1-x} symmetric cell during the first three cycles; (c) EIS spectra of symmetric cells using ZnS_{1-x}, ZnS and ZIF-8 as electrodes; (d-f) CV curves of symmetric cells with ZnS_{1-x}, ZnS and ZIF-8 electrodes under different scan rates. (g-i) Li_2S precipitation profiles on ZnS_{1-x}, ZnS and ZIF-8 cathodic surfaces.

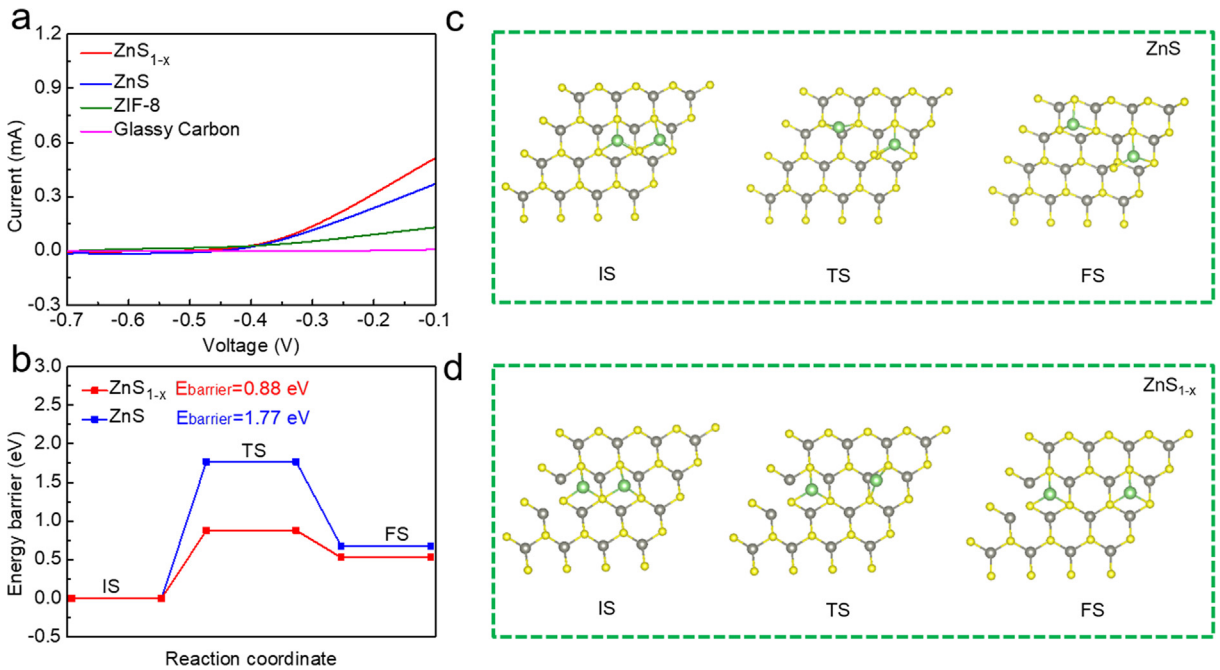

Fig. 8. (a) Li_2S oxidization LSV profiles of ZnS_{1-x}, ZnS and ZIF-8; (b) Li_2S decomposition energy profiles and (c,d) geometrical configurations of Li_2S decomposition on ZnS and ZnS_{1-x} surfaces.

ZnS and ZnS_{1-x} surfaces. The electrocatalytical experiments and DFT calculation strongly verify that the sulfur vacancies in ZnS_{1-x} can enhance LiPSs redox conversion kinetics.

4. Conclusions

In conclusion, we fabricate sulfur-deficient ZnS_{1-x} hollow polyhedrons as the functional sulfur cathode material for Li-S batteries through the simple sulfurization and calcination method. This distinctive hollow structure can efficiently inhibit the volume variation of sulfur upon the lithiation process and physically prevent the diffusion of LiPSs. Furthermore, defect engineering endows the ZnS_{1-x} with enhanced electronic conductivity, improved LiPSs adsorbability, and excellent electrocatalytic activity, thus constructing a multifunctional cathode that effectively inhibits LiPSs shuttling and accelerates the LiPSs conversion kinetics. Thus, the S/ZnS_{1-x} cathode can manifest the favorable reversible capacity, superior rate performance and stable cycling capability. This design could achieve both adsorption and catalysis functions by defect engineering, and provide an inspiration in the development of high-performance Li-S batteries.

Declaration of Competing Interest

The authors declare that they have no known competing financial interests or personal relationships that could have appeared to influence the work reported in this paper.

Acknowledgements

This work was supported by Natural Science Foundation of Hebei Province of China (B2020202052; B2021202028); Outstanding Youth Project of Guangdong Natural Science Foundation (2021B1515020051); State Key Laboratory of Reliability and Intelligence of Electrical Equipment, Hebei University of Technology, China (EERI_PI2020007); the Program for the Outstanding Young Talents of Hebei Province, China (YG.Z.); Chunhui Project of Ministry of Education of the People's Republic of China (No. Z2017010); Department of Science and Technology of Guangdong Province (No. 2020B0909030004); Guangdong Innovative and Entrepreneurial Team Program (No. 2016ZT06C517); Science and Technology Program of Guangzhou (No. 2019050001); Science and Technology Program of Zhaoqing (No. 2019K038).

Appendix A. Supplementary material

Supplementary data to this article can be found online at https://doi.org/10.1016/j.matdes.2021.110060.

References

[1] H. Wu, L. Xia, J. Ren, Q. Zheng, C. Xu, D. Lin, A high-efficiency N/P co-doped graphene/CNT@porous carbon hybrid matrix as a cathode host for high performance lithium-sulfur batteries, J. Mater. Chem. A 5 (2017) 20458–20472, https://doi.org/10.1039/C7TA06504C.
[2] W.X. Shen, J.H. Zang, H. Hu, J.M. Xu, Z.F. Zhang, R.Q. Yan, S.G. Dai, Controlled synthesis of KCu_7S_4/rGO nanocomposites for electrochemical energy storage, Mater. Des. 195 (2020), https://doi.org/10.1016/j.matdes.2020.108992 108992.
[3] B. Liu, R. Fang, D. Xie, W. Zhang, H. Huang, Y. Xia, X. Wang, X. Xia, J. Tu, Revisiting scientific issues for industrial applications of lithium-sulfur batteries, Energy Environ. Mater. 1 (2018) 196, https://doi.org/10.1002/eem2.12021.
[4] M. Chen, Q. Lu, S. Jiang, C. Huang, X. Wang, B. Wu, K. Xiang, Y. Wu, MnO_2 nanosheets grown on the internal/external surface of N-doped hollow porous carbon nanospheres as the sulfur host of advanced lithium-sulfur batteries, Chem. Eng. J. 335 (2018) 831–842, https://doi.org/10.1016/j.cej.2017.11.039.
[5] H. Pan, X. Huang, R. Zhang, D. Wang, Y. Chen, X. Duan, G. Wen, Titanium oxide Ti_3C_2 hybrids as sulfur hosts in lithium-sulfur battery: fast oxidation treatment and enhanced polysulfide adsorption ability, Chem. Eng. J. 358 (2019) 1253–1261, https://doi.org/10.1016/j.cej.2018.10.026.
[6] S. Rehman, K. Khan, Y. Zhao, Y. Hou, Nanostructured cathode materials for lithium-sulfur batteries: progress, challenges and perspectives, J. Mater. Chem. A 5 (2017) 3014–3038, https://doi.org/10.1039/C6TA10111A.
[7] S. Zeng, L. Li, L. Xie, D. Zhao, N. Zhou, N. Wang, S. Chen, Graphene-supported highly crosslinked organosulfur nanoparticles as cathode materials for high-rate, long-life lithium-sulfur battery, Carbon 122 (2017) 106–113, https://doi.org/10.1016/j.carbon.2017.06.036.
[8] M. Chen, S. Jiang, S. Cai, X. Wang, K. Xiang, Z. Ma, P. Song, A.C. Fisher, Hierarchical porous carbon modified with ionic surfactants as efficient sulfur hosts for the high-performance lithium-sulfur batteries, Chem. Eng. J. 313 (2017) 404–414, https://doi.org/10.1016/j.cej.2016.12.081.
[9] W. Yang, W. Yang, L. Dong, X. Gao, G. Wang, G. Shao, Enabling immobilization and conversion of polysulfides through a nitrogen-doped carbon nanotubes/ultrathin MoS_2 nanosheet core-shell architecture for lithium-sulfur batteries, J. Mater. Chem. A 7 (2019) 13103–13112, https://doi.org/10.1039/C9TA03227D.
[10] W. Kang, N. Deng, J. Ju, Q. Li, D. Wu, X. Ma, L. Li, M. Naebe, B. Cheng, A review of recent developments in rechargeable lithium-sulfur batteries, Nanoscale 8 (2016) 16541, https://doi.org/10.1039/C6NR04923K.
[11] M. Yu, J. Ma, M. Xie, H. Song, F. Tian, S. Xu, Y. Zhou, B. Li, D. Wu, H. Qiu, R. Wang, Freestanding and sandwich-structured electrode material with high areal mass loading for long-life lithium-sulfur batteries, Adv. Energy Mater. 7 (2017) 1602347. https://doi.org/10.1002/aenm.201602347.
[12] G.Y. Xu, D.W. Yu, D.C. Zheng, S.J. Wang, W.J. Xue, X.K.E. Cao, H.X. Zeng, X.H. Xiao, M.Y. Ge, W.K. Lee, M.F. Zhu, Fast Heat Transport Inside Lithium-Sulfur Batteries Promotes Their Safety and Electrochemical Performance, Iscience 23 (2020), https://doi.org/10.1016/j.isci.2020.101576 101576.
[13] Y.Z. Luo, Y.Q. Wan, J. Huang, B.Y. Li, Nanofiber enhanced grapheme-elastomer with unique biomimetic hierarchical structure for energy storage and pressure sensing, Mater. Des. 203 (2021), https://doi.org/10.1016/j.matdes.2021.109612 109612.
[14] F.G. Sun, J.T. Wang, D.H. Long, W.M. Qiao, L.C. Ling, C.X. Lv, R. Cai, A high-rate lithium-sulfur battery assisted by nitrogen-enriched mesoporous carbons decorated with ultrafine La_2O_3 nanoparticles, J. Mater. Chem. A 1 (2013) 13283–13289, https://doi.org/10.1039/C3TA12846F.
[15] Y. Zhang, M. Li, S.K. Zhong, Y.L. Sui, X.P. Zhang, X.Y. Li, L. Wu, MoS_2 wrapped MOFs-derived N-doped carbon nanorods as an effective sulfur host for high-performance lithium-sulfur batteries, Ceram. Int. 46 (2020) 9614–9621, https://doi.org/10.1016/j.ceramint.2019.12.227.
[16] T. Meng, J.C. Gao, Y.N. Liu, J.H. Zhu, H. Zhang, L. Ma, M.W. Xu, C.M. Li, J. Jiang, Highly puffed Co_9S_8/Carbon nanofibers: a functionalized s carrier for superior Li-S batteries, ACS Appl. Mater. Inter. 11 (2019) 26798–26806, https://doi.org/10.1021/acsami.9b06497.
[17] Z.H. Sun, J.Q. Zhang, L.C. Yin, G.J. Hu, R.P. Fang, H.M. Cheng, F. Li, Conductive porous vanadium nitride/graphene composite as chemical anchor of polysulfides for lithium-sulfur batteries, Nat. Commun. 8 (2017) 14627, https://doi.org/10.1038/ncomms14627.
[18] D.R. Deng, F. Xue, Y.J. Jia, J.C. Ye, C.D. Bai, M.S. Zheng, Q.F. Dong, Co_4N nanosheet assembled mesoporous sphere as a matrix for ultrahigh sulfur content lithium-sulfur batteries, ACS Nano 11 (6) (2017) 6031–6039, https://doi.org/10.1021/acsnano.7b01945.
[19] Y. Fu, J. Hu, Q. Wang, D. Iin, K. Li, L. Zhou, Thermally etched porous carbon cloth catalyzed by metal organic frameworks as sulphur hosts for lithium-sulfur batteries, Carbon 150 (2019) 76, https://doi.org/10.1016/j.carbon.2019.05.008.
[20] K. Chen, Z. Sun, R. Fang, Y. Shi, H.M. Cheng, F. Li, Metal-Organic Frameworks (MOFs)-Derived Nitrogen-Doped Porous Carbon Anchored on Graphene with Multifunctional Effects for Lithium-Sulfur Batteries, Adv. Funct. Mater. (2018) 1707592, https://doi.org/10.1002/adfm.201707592.
[21] D.Y. Zhu, G.Y. Xu, M. Barnes, Y.L. Li, C.P. T. seng, Z.Q. Zhang, J.J. Zhang, Y.F. Zhu, S. Khalil, M. M. Rahman, R. Verduzco, P. M. Ajayan, Covalent Organic Frameworks for Batteries, Adv. Funct. Mater. (2021) 2100505. https://doi.org/10.1002/adfm.202100505.
[22] M.R. Zhang, X.D. Song, M. Yao, C. Hao, J.S. Qiu, Design Principles for Covalent Organic Frameworks to Achieve Strong Heteroatom-Synergistic Effect on Anchoring Polysulfides for Lithium-Sulfur Batteries, J. Phys. Chem. Lett. 10 (2019) 7445–7451, https://doi.org/10.1021/acs.jpclett.9b02457.
[23] T. Chen, Z. Zhang, B. Cheng, R. Chen, Y. Hu, L. Ma, G. Zhu, J. Liu, Z. Jin, Self-templated formation of interlaced carbon nanotubes threaded hollow Co_3S_4 nano-boxes for high-rate and heat-resistant lithium-sulfur batteries, J. Am. Chem. Soc. 139 (36) (2017) 12710–12715, https://doi.org/10.1021/jacs.7b06973.
[24] X. Liu, P. Chen, J. Chen, Q.H. Zeng, Z.N. Wang, Z.X. Li, L.Y. Zhang, A nitrogen-rich hyperbranched polymer as cathode encapsulated material for superior long-cycling lithium-sulfur batteries, Electrochim. Acta 330 (2020), https://doi.org/10.1016/j.electacta.2019.135337 135337.
[25] Y. Tian, G. Li, Y. Zhang, D. Luo, X. Wang, Y. Zhao, H. Liu, P. Ji, X. Du, J. Li, Low-bandgap Se-deficient antimony selenide as a multifunctional polysulfide barrier toward high-performance lithium-sulfur batteries, Adv. Mater. 32 (2020) 1904876, https://doi.org/10.1002/adma.201904876.
[26] B. Li, S.M. Li, J.H. Liu, B. Wang, S.B. Yang, Vertically aligned sulfur-graphene nanowalls on substrates for ultrafast lithium-sulfur batteries, Nano lett. 5 (2015) 3073–3079, https://doi.org/10.1021/acs.nanolett.5b00064.
[27] Y.K. Yi, Z.C. Liu, P. Yang, T. Wang, X.W. Zhao, H.Y. Huang, Y.H. Cheng, J.Y. Zhang, M.T. Li, MoS_2 nanorods with inner caves through synchronous encapsulation

of sulfur for high performance Li-S cathodes, J. Energ. Chem. 45 (2020) 18–24, https://doi.org/10.1016/j.jechem.2019.09.032.
[28] X.Q. Zhu, J. Li, R.N. Ali, M. Huang, P. Liu, B. Xiang, Toward a high-performance Li-ion battery: Constructing a $Co_{1-x}S$/ZnS@C composite derived from metal-organic framework @3D disordered polystyrene sphere template, Mater. Des. 160 (2018) 636–641, https://doi.org/10.1016/j.matdes.2018.10.011.
[29] X.L. Lu, Q.F. Zhang, J. Wang, S.H. Chen, J.M. Ge, Z.M. Liu, L.L. Wang, H.B. Ding, D. C. Gong, H.G. Yang, J. Zhu, B.G. Lu, High-performance bimetal sulfides for lithium-sulfur batteries, Chem. Eng. J. 358 (2019) 955–961, https://doi.org/10.1016/j.cej.2018.10.104.
[30] L. Ma, S. Wei, H.L. Zhuang, K.E. Hendrickson, R.G. Hennig, L.A. Archer, Hybrid cathode architectures for lithium batteries based on TiS_2 and sulfur, J. Mater. Chem. A 3 (2015) 19857–19866, https://doi.org/10.1039/C5TA06348E.
[31] H.H. Xu, A. Manthiram, Hollow Cobalt Sulfide Polyhedra-enabled Long-life, High Areal-capacity Lithium-Sulfur Batteries, Nano Energy 33 (2017) 124–129, https://doi.org/10.1016/j.nanoen.2017.01.007.
[32] M.e. Zhong, J. Guan, Q. Feng, X. Wu, Z. Xiao, W. Zhang, S. Tong, N. Zhou, D. Gong, Accelerated polysulfide redox kinetics revealed by ternary sandwich-type S@Co/N-doped carbon nanosheet for high-performance lithium-sulfur batteries, Carbon 128 (2018) 86-96. https://doi.org/10.1016/j.carbon.2017.11.084.
[33] W.L. Huang, Z.J. Lin, H.T. Liu, R. Na, J.H. Tian, Z.Q. Shan, Enhanced Polysulfide Redox Kinetics Electro-Catalyzed by Cobalt Phthalocyanine for Advanced Lithium-Sulfur Batteries, J. Mater. Chem. A 6 (2018) 17132–17141, https://doi.org/10.1039/C8TA04890H.
[34] Z. Li, H.B. Wu, X.W. Lou, Rational Designs and Engineering of Hollow Micro-/Nanostructures as Sulfur Hosts for Advanced Lithium-Sulfur Batteries, Energy Environ. Sci. 9 (2016) 3061–3070, https://doi.org/10.1039/C6EE02364A.
[35] M.A. Pope, I.A. Aksay, Structural design of cathodes for Li-S batteries, Adv. Energy Mater. 5 (2015) 1500124, https://doi.org/10.1002/aenm.201500124.
[36] H.C. Wang, C.Y. Fan, Y.P. Zeng, X.H. Zhang, W.H. Li, S.Y. Liu, H.Z. Sun, J. Zhang, L. N. Sun, X.L. Wu, Oxygen-Deficient Titanium Dioxide Nanosheets as More Effective Polysulfide Reservoirs for Lithium-Sulfur Batteries, Chem-Eur. J. 23 (2017) 9666–9673, https://doi.org/10.1002/chem.201701580.
[37] Y.Y. Zhao, W.L. Cai, Y.T. Fang, H.S. Ao, Y.C. Zhu, Y.T. Qian, Sulfur-deficient TiS_{2-x} for promoted polysulfides redox conversion in lithium-sulfur battery, ChemElectroChem. 6 (2019) 2231–2237, https://doi.org/10.1002/celc.201900269.
[38] H.E. Wang, X.C. Li, N. Qin, X. Zhao, H. Cheng, G.Z. Cao, W.J. Zhang J. Sulfur-deficient MoS2 grown inside hollow mesoporous carbon as a functional polysulfide mediator, J. Mater. Chem. A 19 (2019) 12068-12074. https://doi.org/10.1039/C9TA01722D
[39] M.M. Liu, C.C. Zhang, J.M. Su, X. Chen, T.Y. Ma, T. Huang, A.S. Yu, Propelling Polysulfide Conversion by Defect-Rich MoS_2 Nanosheets for High-Performance Lithium-Sulfur Batteries, ACS Appl. Mater. Inter. 11 (2019) 20788–20795, https://doi.org/10.1021/acsami.9b03011.
[40] H.B. Lin, L.Q. Yang, X. Jiang, G.C. Li, T.R. Zhang, Q.F. Yao, G.Y.W. Zheng, J.Y. Lee, Electrocatalysis of polysulfide conversion by sulfur-deficient MoS_2 nanoflakes for lithium-sulfur batteries, Energy Environ. Sci. 10 (2017) 1476–1486, https://doi.org/10.1039/c7ee01047h.
[41] F.X. Xie, L. Zhang, Q.F. Gu, D.L. Chao, M. Jaroniecc, S.Z. Qiao, Multi-shell hollow structured Sb_2S_3 for sodium-ion batteries with enhanced energy density, Nano Energy 60 (2019) 591–599, https://doi.org/10.1016/j.nanoen.2019.04.008.
[42] Z. Jiang, H. Sun, Z. Qin, X. Jiao, D. Chen, Synthesis of novel ZnS nanocages utilizing ZIF-8 polyhedral template, Chem. Commun. 48 (2012) 3620–3622, https://doi.org/10.1039/C2CC00004K.
[43] R. Razaqa, D. Sun, J. Wang, Y. Xin, G. Abbas, J.H. Zhang, Q. Lia, T.Z. Huang, Z.L. Zhang, Y.H. Huang, Ultrahigh sulfur loading in ZnS_{1-x}/rGO through in situ oxidation-refilling route for high-performance Li-S batteries, J. Power Sources 414 (2019) 453–459, https://doi.org/10.1016/j.jpowsour.2019.01.038.